Soft Matter

ARTICLE TYPE

Cite this: DOI: 10.1039/D1SM01141C

Supplementary Information for: A few upstream bifurcations drive the spatial distribution of red blood cells in model microfluidic networks

Adlan Merlo,‡ Maxime Berg,‡ Paul Duru, Frédéric Risso, Yohan Davit, and Sylvie Lorthois

SIA. Supplementary results: Multiple equilibria in microvascular networks

The problem formed by Eqs. 6-17 is non-linear and may therefore have several equilibrium solutions. Karst et al. showed, using continuation methods, that for blood flow in 2D Voronoi-like networks, the number of equilibria was an increasing function of the inlet tube hematocrit, although they noted that such equilibria were lying close to each other[1]. However, they used a customized phase separation relationship along with the expression for the effective viscosity of the blood deduced from in vivo experiments. In particular, the latter induces a much stronger feedback of the RBC on the flow compared to the in vitro expression used in this work, and this feedback is a key in the emergence of multiple equilibria.

Given the low inlet tube hematocrit considered ($H_t^i = 0.035$) and the weak feedback of the RBC on the flow (see Fig. 3b), we suspect that the discrepancies between experiments and simulations highlighted in Fig. 3a cannot come from our numerical method converging towards to a wrong solution. Still, we tried, using the numerical method presented in Section SID (Eqs. SI.4 to SI.8) to trigger different equilibrium solutions in the hexagonal network. To do so, we introduced a relaxation factor $0 < \gamma \leq 1$ so that

$$H_{d,ij}^{n+1} = \gamma H_{d,ij}^{s} + (1-\gamma) H_{d,ij}^{n}, \tag{SI.1}$$

where H_d^s represents the solution of the system formed by equations SI.4 and SI.8. This relaxation factor is a free parameter and allows us to control the convergence of the numerical method. We then solved the blood flow problem for an increasing inlet tube hematocrit (from $H_{t,\text{inlet}} = 0$ to $H_{t,\text{inlet}} = 0.9$). For each value of the inlet tube hematocrit and for an increasing relaxation parameter value (from $\gamma = 0.01$ to $\gamma = 1$), we solved the blood flow problem starting from the same 20 initial tube hematocrit distributions. We constructed each one of these initial tube hematocrit distributions by sampling the hematocrit of each segment (excluding inlets) from a uniform distribution so that $H_{t,\text{initial}} \sim \mathscr{U}(0,1)$. Such a screening procedure can be seen as a very crude numerical continuation method[2].

To make sure that this screening procedure was capable of capturing different equilibria, we applied it first in ladder-like networks (Figure SI1), similar in topology to the hexagonal network depicted in Figure 2, but with an increased number of inlets and outlets. These networks were prescribed with uniform tube hematocrit at the inlets (red segments in Fig. SI1a) and uniform pressure drops between inlets and outlets (blue lines in Figure SI1a). Given their geometries and the boundary conditions prescribed, such networks always exhibit at least one trivial equilibrium regardless of the inlet tube hematocrit, which is no flow in horizontal segments and uniform flow and tube hematocrit in the vertical segments. Figure SI1b, which displays the tube hematocrit in the horizontal segment highlighted by a black arrow in Fig. SI1a, shows that in ladder networks, beyond a certain inlet tube hematocrit, this trivial equilibrium becomes unstable and more equilibria start to emerge. We note that this threshold is a decreasing function of the network size so that the trivial equilibrium, in large network, starts to destabilize for lower initial tube hematocrits. For ladder networks with the same size as the hexagonal network, we found that this threshold lies around $H_{t,\text{inlet}} \approx 0.8 \pm 0.05$, which is considerably larger than the range of inlet tube hematocrit explored experimentally in this work. Finally, we note that similar destabilizations were already obtained using a Wheatstone bridge-like network, with even the emergence of oscillations[3]. This shows that our screening procedure was able to capture, to some extent, different equilibria.

We repeated this procedure on the hexagonal network and the method did not converge towards more than one equilibrium, regardless of the inlet tube hematocrit considered. This does not definitely rule out the existence of several equilibria associated with the hexagonal network at low inlet tube hematocrit, however it strongly suggests that if they exist, such solutions are likely to be very close to each other and therefore cannot explain the difference observed between experiments and simulations in Fig. 3a.

SIB. Supplementary results: Tissue Fåhraeus effect

The tissue Fåhraeus effect (TFE) denotes a reduction of the volume fraction of RBCs in the whole network by comparison to its

Institut de Mécanique des Fluides de Toulouse, IMFT, Université de Toulouse, CNRS, Toulouse, France

‡ These authors contributed equally to this work

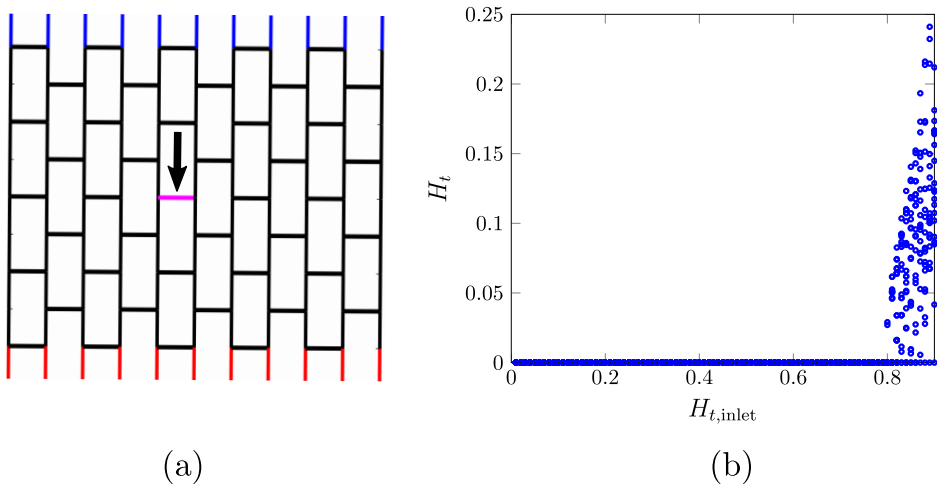

Figure SI1 Multiple equilibria in a ladder network ($W = 10\mu m$). (a) Ladder network with inlets highlighted in red and outlets in blue. (b) Tube hematocrit in the purple horizontal segment highlighted by the black arrow in (a) as a function of inlet hematocrit.

discharge hematocrit (defined as the ratio between the RBC flow and the total flow)[4,5]:

$$TFE = \frac{\mathscr{V}_{RBC}}{\mathscr{V}} \frac{1}{H_d^i} = \frac{\mathscr{V}_{RBC}}{\mathscr{V}} \frac{Q_{RBC}^i}{Q^i},$$

where $\mathscr{V}_{RBC}$ is the total volume of RBCs within the network ($\mathscr{V}_{RBC} = \sum_k H_{t,k} \pi L_k r_k^2$), $\mathscr{V}$ is the total volume of the network ($\mathscr{V} = \sum_k \pi L_k r_k^2$) and H_d^i, Q_{RBC}^i and Q^i are the discharge hematocrit, the flow rate of RBCs and the total flow rate at the network inlet, respectively. It is analogous to the Fåhraeus effect, {i.e.}, the reduction of the hematocrit within a single segment (tube hematocrit) by comparison to the discharge hematocrit ($FE_k = {}^{H_{t,k}}/_{H_{d,k}}$). The latter results from the correlation between hematocrit and velocity within a single vessel cross-section[4,6], which can be evidenced by rewriting the Fåhraeus effect as the ratio between the RBC average transit time and the total average transit time throughout this vessel. Similarly, the tissue Fåhraeus effect can be expressed as the ratio between the RBC average travel time and the total average travel time throughout the network, and thus results from the correlation between high velocity and high hematocrit vessels.

Fig. SI2 displays the tube hematocrit as a function of RBC velocity in each channel of the hexagonal network, as predicted by the equivalent fluid network model, without correcting phase separation at order-1 bifurcations (red circles) and after correcting phase separation at order-1 bifurcations, as described in Sections 2.4 and 2.5. Except for the channels with the highest velocities (i.e. inlet channel and daughter channels of the order-0 bifurcation), where it does not change the tube hematocrit, this correction increases the tube hematocrit in all channels with a normalized velocity larger than ~ 0.2 and decreases the tube hematocrit in all channels with a normalized velocity larger than ~ 0.05, thus increasing the correlation between high velocity and high hematocrit channels. This results in a $\sim 10\%$ reduction of the value of TFE, corresponding to an increase of the tissue Fåhraeus effect.

SIC. Supplementary Results: RBC distribution in the hexagonal network with narrow channels

Experiments in such networks are extremely difficult to perform because RBCs quickly clog some channels despite the treatment of our microfluidic devices with BSA to reduce RBC adhesion at walls. This prevented from getting stable flow fields and RBC distributions over sufficient periods of time to extract quantitative measures of both the flow rate and hematocrit throughout the network. However, because the strong confinement induces a fast relaxation of RBCs toward the channel center at each bifurcation, the RBC distribution can be deduced using the equivalent fluid model described in Section 6.2. Figure SI3 shows the

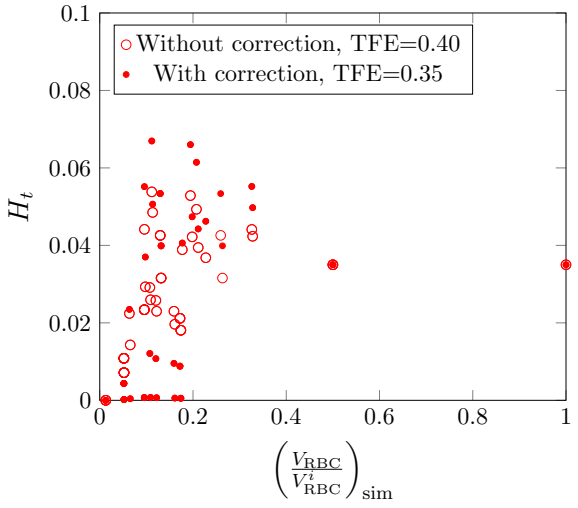

Figure SI2 Tube hematocrit as a function of red blood cell velocity in each segment of the hexagonal network, as predicted by the equivalent fluid network model, with (red dots) and without (red circles) correcting phase separation at order-1 bifurcations as described in Sections 2.4 and 2.5 ($W = 10\mu m$ and $H_t^i =$). For each scenario, the value of the tissue Fåhraeus effect is given in the legend.

corresponding simulated RBC distribution. Once again, the central region of the network is favored even if the heterogeneity at large scale is reduced compared to the simulation for large channels (see Fig. 7b for comparison). This same phenomenon arises when increasing the inlet tube hematocrit in the network with larger channels (simulations not shown).

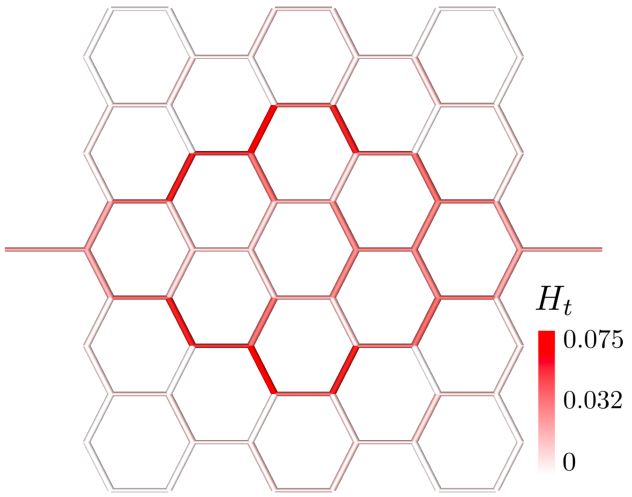

Figure SI3 Distribution of simulated tube hematocrit in a hexagonal network made of 5μm-wide channels with $H_t^i = 0.035$.

SID. Supplementary results: Structure of the baseline flow field in hexagonal and square networks

For flow in networks with channels of equal sizes, the structure of the baseline flow field can generally be inferred from the length of the flow pathways that connect the network inlet and outlet. For imposed inlet and outlet pressures, it is obvious that the pressure drop per unit length along a given pathway is inversely proportional to the length of this pathway, so that higher flow rates are expected on shorter pathways.

In the hexagonal network, the length of flow pathways that connect the network inlet and outlet is much shorter for pathways visiting the network center (see e.g. blue line in Fig. SI4, left panel), while they are longer for pathways visiting the network periphery (see e.g. orange trajectory in Fig. SI4, left panel). Thus, the pressure drop by unit length is smaller in the peripheral pathways compared to the central one, resulting in a smaller flow rate in branch β compared to branch α. Consistently, solving for the baseline flow field in this network yields $\frac{Q^\beta}{Q^\alpha} = 0.5803$ so that $\frac{l_{center}}{l_{periphery}} = 11/19 = 0.5789$ provides a good approximation for this flow ratio. A similar result would of course be obtained in a square network with a single inlet and outlet located in the center of opposite sides.

In the square network, however, the length of the peripheral pathways is equal to the length of the central ones (see e.g. orange vs. blue trajectory in Fig. SI4, right panel). As a result, the above rough approximation yields $\frac{Q^\beta}{Q^\alpha} = 1/2$, making it impossible to predict the branch with the highest flow. To go further, let consider the formal analogy between :

- the baseline pressure field in the square network, i.e. the solution of Eqs. 6 and 8 with uniform effective viscosity and imposed pressures ($P_i = 1$ and $P_o = 0$) at the inlet and outlet , respectively

- and the solution of the Laplace equation discretized with a finite-difference scheme over a square region with the following boundary conditions: imposed pressures at the lower-left and upper-right corner, and Neumann boundary-conditions ($\vec{\nabla} P.\vec{n} = 0$) everywhere else on the boundary.

Because isopressures and streamlines of the later are orthogonal to each other, we can deduce that isopressures are locally orthogonal to the domain boundaries, which are evident streamlines. Thus, the concavity of isopressures ($P \geq 0.5$) must be oriented toward the lower left corner, as schematized by the red dotted line in the right panel of Fig. SI4, and the concavity of isopressures ($P \leq 0.5$) must be oriented toward the upper right corner*. This yields a higher pressure drop, resulting in a larger flow rate, in branch β than in branch α.

SIE. Supplementary methods: Experiments

We compute the optical density profile OD(x) from the time-averaged grey-scale intensity profile $I(x)$ as follows[7–11]:

$$\mathrm{OD}(x) = -\log_{10}\left(\frac{I(x)}{I_{0(x)}}\right), \qquad \text{(SI.2)}$$

where $I_0(x)$ is a reference intensity profile. Following Sherwood et al.[9], we assume that $I_0(x)$ is constant and equal to the grey-scale value in the PDMS far from any channel, as illustrated in Fig. SI3a. This is a reasonable approximation except in the close vicinity of the channel walls (see line transverse to the channel axis, where the channel is devoid of RBCs, highlighted in Fig. SI3a). Channel walls result in strong fluctuations of the intensity, with two bright stripes located outside the channel walls, resulting in peaks of high intensity as shown in Fig. SI3b. We assume these peaks are at equal distance to the channel center, and then determine the channel wall locations by translation ($\pm W/2$). Moreover, we discard the optical signatures of these channels walls, which appear in the time-averaged grey-scale intensity image (Fig. SI3c) and in the optical density profile, as shown by dotted lines in Fig. SI3d. More precisely, starting from the channel center, we only keep the positive optical density values, as in the left hand side of the channel, or the values encountered before the first local minimum, as in the right hand side of the channels. The hematocrit profile is then estimated as follows (Fig. SI3e): in the central region, it is deduced by calibration from the Optical Density value (see below); on the side where negative values of the Optical Density have been discarded, it is assumed to be null, on the side where a local minimum has been reached, it is inferred from the optical density profile by linear extrapolation.

We calibrated the relationship between the local optical density and the local depth-averaged hematocrit by using Leja slides (Leja Products B.V.). These are manufactured Hele-Shaw cells

* resulting in the isopressure line ($P = 0.5$) being the upper-left to lower-right diagonal.

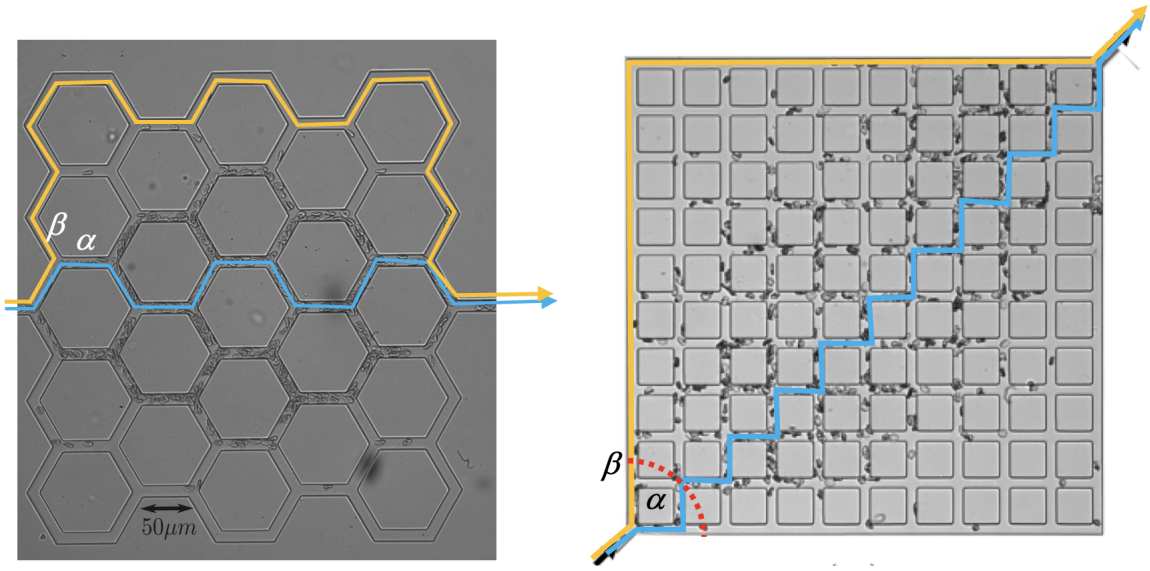

Figure SI4 Examples of central (blue) and peripheral (orange) trajectories in the hexagonal (left) and square (right) configuration. Consistent with the notations used in the manuscript, α denotes the daughter branch of order-1 bifurcations located on the same side than the previous, order-0, bifurcation apex. The red dotted line schematizes the isopressure line corresponding to α downstream vertex.

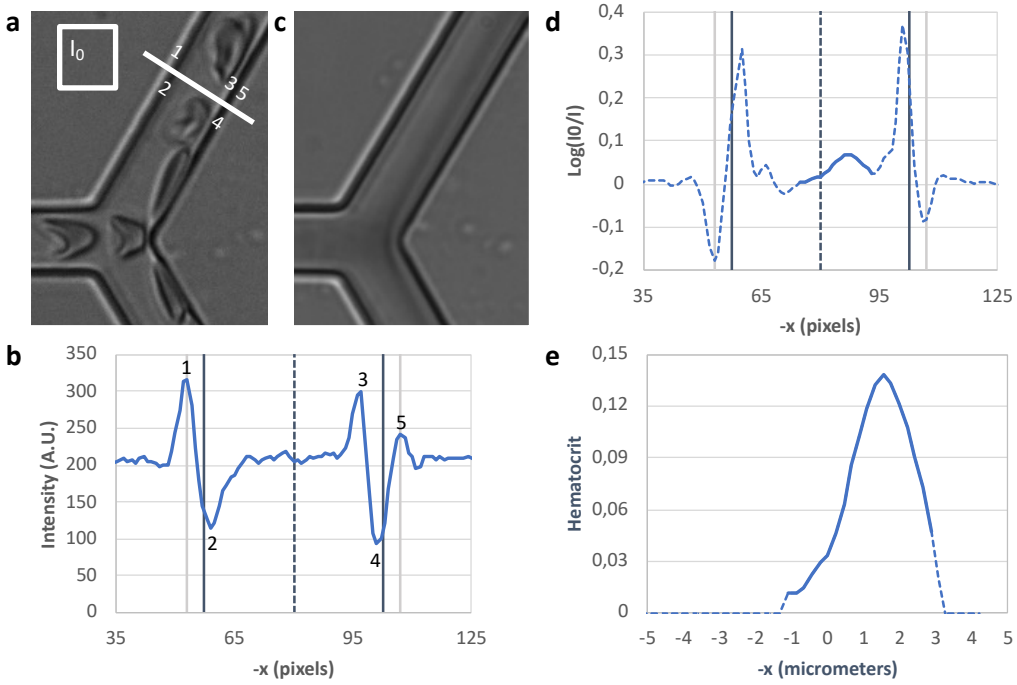

Figure SI5 Experimental determination of hematocrit profiles in channels with square cross-sections of $10 \times 10 \mu m^2$. a: Instantaneous snapshot showing a typical area used for estimating the average background intensity I_0 and a line transverse to the channel axis, where the channel is devoid of RBCs. Labels 1, 3 and 5 highlight the bright stripes induced by channel walls and labels 2 and 4 highlight the dark stripes; b: Instantaneous intensity profile (Arbitrary Units) associated to the transverse line highlighted in Panel a. The two outermost peaks (grey continuous lines) correspond to stripes 1 and 5 in Panel a, and are assumed to be at equal distance to the channel center (dashed line). Locations of the channel walls (black continuous lines) are deduced from the channel center by translation $(\pm W/2)$; c: Intensity I averaged over 3 seconds, keeping one of ten snapshots to avoid considering the same RBC multiple times at the same location. d. Optical Density (blue) profile on the same line as in Panel b, estimated as $Log(I/I_0)$. Dashed lines highlight the locations where the Optical Density is perturbed by the vessel walls, while the continuous line highlights the locations where we consider it is proportional to the hematocrit, according to the calibration displayed in Fig. SI4; e. Hematocrit, directly obtained from the measured Optical Density and the calibration curve shown in Fig. SI6 (continuous line) or inferred by linear interpolation and replacement of negative values by zero (dashed line).

with finely controlled depths (10 or 20μm) and much larger length and width ($\sim 2cm$). We filled each slide extremely slowly with a small volume of RBC suspension of known feed hematocrit, so as to reduce as much as possible local hematocrit heterogeneities within the slide, while ensuring it contained the whole injected volume. In that way, the local hematocrit is everywhere equal to the feed hematocrit, which enables precise calibration of the optical density, even for suspensions where RBCs are not individually discernible. As expected from Beer-Lambert law, the slope of the linear regressions obtained for moderate hematocrit values in 20μm Leja slides is twice the slope obtained in 10μm Leja slides. Also, the results obtained in the present work match those obtained previously in 20μm-side channels with the same imaging system, in the limit of small hematocrits, which validates the calibration method.

Finally, we derive the tube hematocrit H_t associated to each microchannel by averaging $H(x)$ over the channel width W at a longitudinal position in the channel where the RBC velocity profile is neither influenced by the previous nor by the next bifurcation ($z = 45\mu$m):

$$H_t = \left[\frac{1}{W} \int_{-W/2}^{W/2} H(x) dx \right]_{z=45\mu\text{m}}. \tag{SI.3}$$

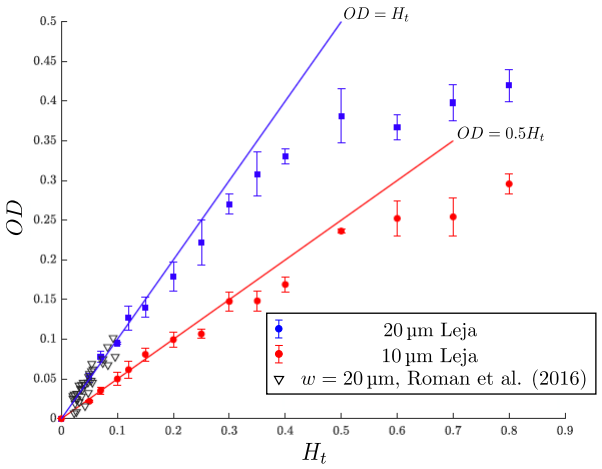

Figure SI6 Calibration of optical density from local depth-averaged hematocrit. Filled symbols: mean and standard deviation for 3 experiments in Leja Slides. Red circles: 10μm depth; Blue squares: 20μm depth. Empty triangles: data obtained by Roman et al.[10] in 20μm side channels for small hematocrits, which can be measured by individually counting the RBCs. Lines: linear regressions for H from 0 to 0.3 (10μm depth) or 0 to 0.15 (20μm depth).

SIF. Supplementary methods: Numerical solving of the blood flow problem

The blood flow model is defined by Eqs. 6-17 and represents a coupled non-linear problem that we solve iteratively. Each iteration is divided into two steps. First, we solve the linear system formed by Eqs. 6 and 8-11, which yields the pressure and total flow rate, using the discharge hematocrit obtained at the previous iteration, so that

$$\sum_j Q_{ij}^{n+1} = 0, \tag{SI.4}$$

$$Q_{ij}^{n+1} = \frac{\pi d_{\text{h},ij}^4}{128 \mu_{\text{eff},ij}(H_{d,ij}^n) L_{ij}} \left(P_i^{n+1} - P_j^{n+1} \right), \tag{SI.5}$$

where $n+1$ represents the current iteration, n the previous iteration and where $\mu_{\text{eff},ij}(H_{d,ij}^n)$ highlights the dependency of the effective viscosity upon the unknowns of the problem. We then use the flow rate solution of the above two equations, to solve Eqs. 7, 12 and 13, which yields the discharge hematocrit so that

$$\sum_j H_{d,ij}^{n+1} Q_{ij}^{n+1} = 0, \tag{SI.6}$$

at all bifurcations and

$$H_{d,\alpha}^{n+1} = \frac{FQ_E^\alpha(H_{d,e}^n, FQ_B^{\alpha,n+1})}{FQ_B^{\alpha,n+1}} H_{d,e}^{n+1}, \tag{SI.7}$$

$$H_{d,\beta}^{n+1} = \frac{1 - FQ_E^\alpha(H_{d,e}^n, FQ_B^{\alpha,n+1})}{1 - FQ_B^{\alpha,n+1}} H_{d,e}^{n+1}, \tag{SI.8}$$

at each diverging bifurcations. We recall that $FQ_B^{\alpha,n+1} = \left| \frac{Q_\alpha^{n+1}}{Q_e^{n+1}} \right|$ and that $FQ_E^\alpha(H_{d,e}^n, FQ_B^{\alpha,n+1})$ is described by Eq. 14. We note that FQ_E^α uses the discharge hematocrit values at the previous iteration ($H_{d,e}^n$), so that Eqs. SI.6 to SI.8 also form a linear system straightforward to solve. This two-step method is justified since RBCs have a relatively weak feedback on the flow (*i.e.* $\frac{\partial \mu_{\text{eff},ij}}{\partial H_{d,ij}}$ is small), especially in the regime of small discharge hematocrit, which is the focus of this work, so that equation SI.5 can be linearized and truncated around $H_{d,ij}^n$.

References

1 N. J. Karst, J. B. Geddes and R. T. Carr, Bulletin of Mathematical Biology, 2017, **79**, 662–681.

2 E. L. Allgower and K. Georg, Numerical Continuation Methods, Springer, Berlin, Heidelberg, 1990.

3 N. J. Karst, B. D. Storey and J. B. Geddes, Bulletin of Mathematical Biology, 2015, **77**, 1377–1400.

4 A. R. Pries and P. Gaehtgens, in Dispersion of Blood Cell Flow in Microvascular Networks, ed. J.-S. Lee and T. C. Skalak, Springer New York, New York, NY, 1989, pp. 50–64.

5 A. R. Pries, T. W. Secomb and P. Gaehtgens, American Journal of Physiology-Heart and Circulatory Physiology, 1995, **269**, H1713–H1722.

6 A. R. Pries, T. W. Secomb and P. Gaehtgens, Cardiovascular Research, 1996, **32**, 654–667.

7 H. H. Lipowsky, S. Usami, S. Chien and R. N. Pittman, Microvascular Research, 1982, **24**, 42 – 55.

8 A. R. Pries, G. Kanzow and P. Gaehtgens, American Journal of Physiology-Heart and Circulatory Physiology, 1983, **245**, H167–H177.

9 J. M. Sherwood, E. Kaliviotis, J. Dusting and S. Balabani, Biomechanics and Modeling in Mechanobiology, 2014, **13**, 259–273.

10 S. Roman, A. Merlo, P. Duru, F. Risso and S. Lorthois, Biomicrofluidics, 2016, **10**, 034103.

11 A. Mantegazza, F. Clavica and D. Obrist, Biomicrofluidics, 2020, **14**, 014101.